Mesoporous Materials Hot Paper

International Edition: DOI: 10.1002/anie.201411791
German Edition: DOI: 10.1002/ange.201411791

2D Zeolite Coatings: Langmuir–Schaefer Deposition of 3 nm Thick MFI Zeolite Nanosheets**

Neel Rangnekar, Meera Shete, Kumar Varoon Agrawal, Berna Topuz, Prashant Kumar, Qiang Guo, Issam Ismail, Abdulrahman Alyoubi, Sulaiman Basahel, Katabathini Narasimharao, Christopher W. Macosko, K. Andre Mkhoyan, Shaeel Al-Thabaiti, Benjamin Stottrup, and Michael Tsapatsis**

Abstract: *Stable suspensions of zeolite nanosheets (3 nm thick MFI layers) were prepared in ethanol following acid treatment, which partially removed the associated organic structure-directing agent. Nanosheets from these suspensions could then be dispersed at the air–water interface and transferred to silicon wafers using Langmuir–Schaefer deposition. Using layer-by-layer deposition, control on coating thickness was demonstrated. In-plane X-ray diffraction (XRD) revealed that the deposited nanosheets contract upon calcination similar to bulk MFI crystals. Different methods for secondary growth resulted in preferentially oriented thin films of MFI, which had sub-12-nm thickness in certain cases. Upon calcination, there was no contraction detectable by in-plane XRD, indicating well-intergrown MFI films that are strongly attached to the substrate.*

2D zeolites, nanosheets with thickness comparable to the unit-cell-dimensions of the corresponding structure type (for a list of structure types see http://www.iza-online.org),[1] open exciting opportunities for traditional uses in catalysis and separations[2–9] and hold promise for emerging applications of zeolite films, such as membranes,[10] low dielectric constant materials,[11,12] and anti-corrosion coatings.[11] Fabrication of thin films of 2D zeolites relies on: 1) the availability of suspensions that exhibit colloidal stability, and are free of amorphous and non-exfoliated contaminants; and 2) development of deposition techniques by which the suspended zeolite nanosheets can be quantitatively transferred on various supports to form oriented thin coatings.

Following the discovery of multilamellar MFI zeolite by Ryoo and co-workers,[3] we used a polymer-melt-compounding technique (for exfoliation) combined with density gradient centrifugation (for purification) to prepare suspensions of exfoliated 2D MFI nanosheets in toluene and octanol.[13,14] In our earlier work, the octanol and toluene suspensions were used to form nanosheet deposits on porous supports by filtration.[13,14] Deposition by filtration ensured transfer of all zeolite nanosheets from the suspension to the surface of the support. Such quantitative transfer from suspension to support, without nanosheet loss, is essential because high-quality 2D zeolites cannot be obtained currently in large quantities. However, the filtration approach is only applicable to porous supports. Furthermore, a uniform coating with thickness on the order of a single layer of nanosheets is not possible by this technique. To overcome these drawbacks, we investigated the application of the Langmuir–Schaefer (LS) deposition technique for the formation of MFI nanosheet coatings.

Deposition from Langmuir trough is a well-known method used to obtain monolayers of surfactant molecules[15–17] and it has been used to deposit particles including zeolites[18–22] and various 2D non-zeolitic materials.[23,24] To employ the LS deposition, we started from an MFI nanosheet suspension in octanol prepared according to our previously reported procedure.[14] The nanosheets were then transferred to ethanol and subjected to an acid treatment procedure, reported earlier by Corma and co-workers for the removal of organic structure-directing agent (OSDA) from zeolites.[25] This acid treatment resulted in partial removal of the long-chain OSDA used in the synthesis of multilamellar MFI and

[*] N. Rangnekar,[+] M. Shete,[+] Dr. K. V. Agrawal, Dr. B. Topuz, P. Kumar, Dr. Q. Guo, I. Ismail, Prof. C. W. Macosko, Prof. K. A. Mkhoyan, Prof. M. Tsapatsis
Department of Chemical Engineering and Materials Science
University of Minnesota, 421 Washington Avenue SE
Minneapolis, MN 55455 (USA)
E-mail: tsapatsis@umn.edu
Prof. B. Stottrup
Department of Physics, Augsburg College
2211 Riverside Avenue, Minneapolis, MN 55454 (USA)
E-mail: stottrup@augsburg.edu
Prof. A. Alyoubi, Prof. S. Basahel, Dr. K. Narasimharao, Prof. S. Al-Thabaiti
Department of Chemistry, Faculty of Science
King Abdulaziz University, Jeddah, 21589 (Saudi Arabia)
[+] These authors contributed equally to this work.

[**] Financial support for this work was provided by the deanship of scientific research at King Abdulaziz University D-003/433 and from the Department of Energy, Office of Basic Energy Sciences, Division of Chemical Sciences, Geosciences and Biosciences under award number DE-FG-02-12ER16362. The Langmuir–Blodgett trough instrumentation purchase and maintenance was supported by the NSF (grant numbers DMR 1207544 and CHE 1040126). K.V.A. acknowledges support by a DDF fellowship granted by the University of Minnesota. B.T. acknowledges support from the Scientific and Research Council of Turkey (TUBITAK, grant number BIDEP-2219). Parts of this work were conducted at the Characterization Facility of the University of Minnesota and the Minnesota Nanocenter (formerly NFC), which receive partial support from the NSF through the MRSEC and NNIN programs, respectively.

Supporting information for this article is available on the WWW under http://dx.doi.org/10.1002/anie.201411791.

allowed for the formation of stable suspensions in ethanol. Nanosheets could then be introduced at the air–water interface, and transferred to silicon wafers by using the Langmuir–Schaefer horizontal lifting technique.[16] Secondary growth of these monolayers resulted in intergrown, preferentially oriented, sub-12-nm films, which were firmly attached to the support and did not show in-plane contraction upon calcination. On the other hand, non-intergrown multilayers could slide and contract upon calcination. The LS deposition provides the opportunity to coat monolayers of 2D zeolites such as MFI and MWW nanosheets. Secondary growth can allow formation of sub-12-nm, crack-free, intergrown zeolite films, of which to the best of our knowledge, there are no reports in the literature.

Following acid treatment (details are given in the Supporting Information), removal of OSDA ($C_{22}H_{45}$-N^+-$(CH_3)_2$-C_6H_{12}-$N^+(CH_3)_2$-C_6H_{13}·$(2\,OH^-)$) was quantitated by thermogravimetric analysis (TGA) of MFI nanosheets. Specifically, the nanosheets recovered by centrifugation were analyzed by TGA after acid treatment and compared with the TGA results prior to acid treatment (see Figure S1 in the Supporting Information). Before acid treatment, the nanosheets contained about 29 wt % OSDA, the majority of which is expected to reside inside their straight pore channels.[14] After acid treatment, the amount of OSDA reduced to less than 8 wt %. The partial removal of OSDA was also indicated by a color change of the solid nanosheet material from yellow to white. We believe that the acid treatment procedure reduces the lipophilicity of nanosheets and allows for their transfer out of octanol to form a stable suspension in ethanol.

Figure 1 a, e show transmission electron microscopy (TEM) images of nanosheets, deposited on carbon-coated copper TEM grids, before and after acid treatment, respectively. Nanosheets deposited from both octanol and ethanol suspensions appeared well dispersed. In contrast, nanosheets suspended in ethanol without acid treatment formed agglomerates (not shown). High-resolution TEM images (Figure 1 b, f) and electron diffraction patterns (Figure 1 c, g) showed that the acid treatment process did not alter their crystal structure. More detailed crystallographic investigation regarding the structural integrity and thickness of the nanosheets was performed by diffraction tilting experiments in the TEM.[26] The experimental and simulation data shown in Figure 1 d, h, confirmed that the nanosheets were 1.5 unit cells thick (which corresponds to approximately 3 nm) and further confirmed that the crystalline structure of MFI was preserved.

Although a major fraction of the OSDA was removed, the remaining OSDA appears to be occluded in the micropores as Ar-adsorption measurements failed to detect any microporosity (data not shown). Moreover, the presence of the remaining OSDA made the nanosheets retain some hydrophobicity which prohibited their dispersion in water.

The dispersed nanosheets in ethanol were transferred to the air–water interface by simply adding droplets of the suspension on the surface of water. Ethanol evaporated or dissolved in water leaving behind the nanosheets which spread on the surface of water. The surface pressure isotherm obtained during a typical LS experiment is shown in Figure 2 a. At large trough areas, the isotherms remained horizontal until, at a certain trough area, a rapid increase in surface pressure was observed because of the onset of interactions between adjacent particles. When a certain minimum trough area (i.e., maximum surface pressure) was reached, the barriers were expanded, and a decrease in surface pressure was observed, which did not follow the surface pressure versus area curve obtained during compression. The slower increase and sharper decline of surface pressure during compression and expansion, respectively, may indicate loss of particles to the water subphase and/or irreversible aggregation of the nanosheets. In what follows, we report nanosheet deposits formed on silicon wafers transferred during the first compression.

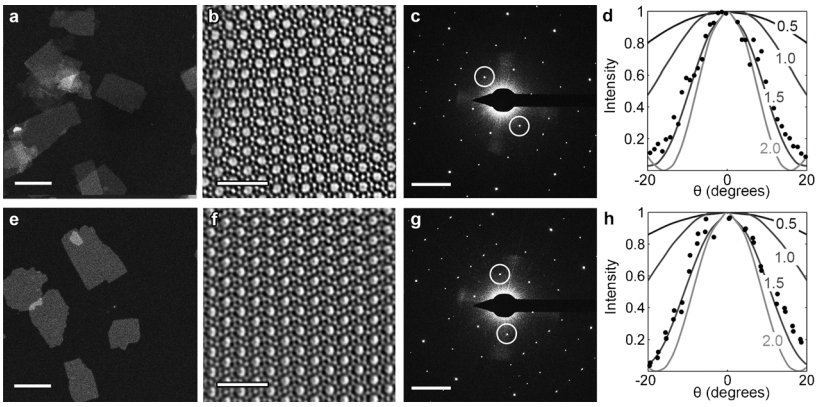

Figure 1. Top row: MFI nanosheets before acid treatment (deposited from octanol). Bottom row: MFI nanosheets after acid treatment (deposited from ethanol). a,e) Low-magnification HAADF-STEM images of MFI nanosheets supported on an ultrathin carbon film showing uniform thickness of nanosheets; scale bars = 500 nm. b,f) High-resolution Bragg-filtered CTEM images of MFI nanosheets; scale bars = 2 nm. c,g) [010] zone axis diffraction pattern with the circles highlighting (101) and (−10−1) spot; scale bars = 1 nm^{-1}. d,h) Multislice simulated modulation of encircled diffraction spots in (c,g) with tilting for nanosheets of different thickness (solid lines) and corresponding experimental scatter data (solid circles) confirming that the nanosheets are 1.5 unit cells thick. For clarity, a larger version of this figure is provided in Figure S2.

Silicon wafers, as-purchased or with a 50 nm thermally-grown oxide layer were used as the substrates for nanosheet coatings. Figure 2 b–d show scanning electron microscopy (SEM) images of the coatings made on thermally oxidized silicon wafers at various surface pressures. Surface coverage of nanosheets increased with increasing surface pressure. Closely packed monolayers were obtained at 20 and 25 $mN\,m^{-1}$ surface pressure while at even higher surface pressures we observed the onset of nanosheet overlapping (Figure S3).

The thickness of a monolayer coating of nanosheets was confirmed by atomic force microscopy (AFM), as shown in Figure 3 a, b. The coating imaged by AFM was deposited at 25 $mN\,m^{-1}$ surface pressure on a thermally oxidized silicon wafer (similar to the coating shown in Figure 2 d). Line profiles across three randomly chosen nanosheets are shown

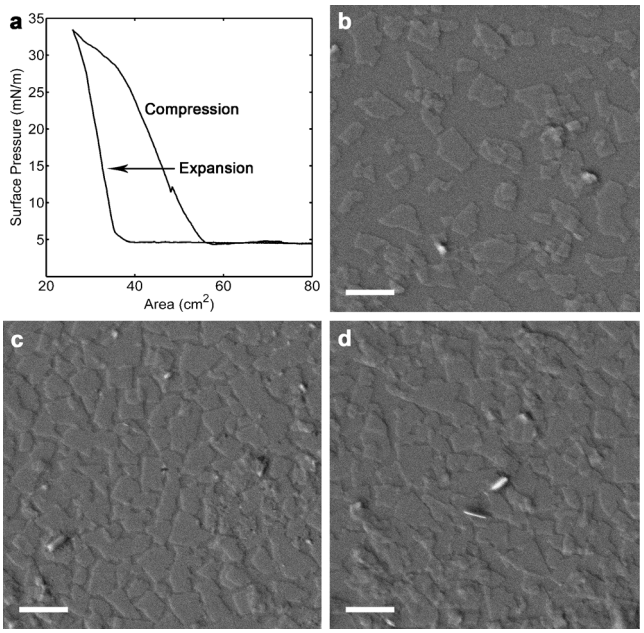

Figure 2. a) Surface pressure isotherm from the first compression–expansion cycle obtained during a typical LS experiment. b–d) Coatings made at 15, 20, and 25 mN m^{-1} surface pressure on thermally oxidized silicon substrates showing that packing of nanosheets increases with surface pressure, eventually resulting in overlapped coatings; scale bars = 400 nm.

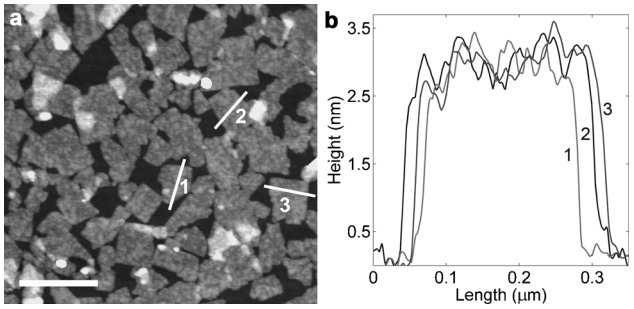

Figure 3. a) AFM image of nanosheets deposited on silicon substrate using LS; scale bar = 500 nm and b) the corresponding height profiles showing that nanosheets are approximately 3 nm in thickness. Calibration was done using 2.0 nm steps on HF-etched mica.[27]

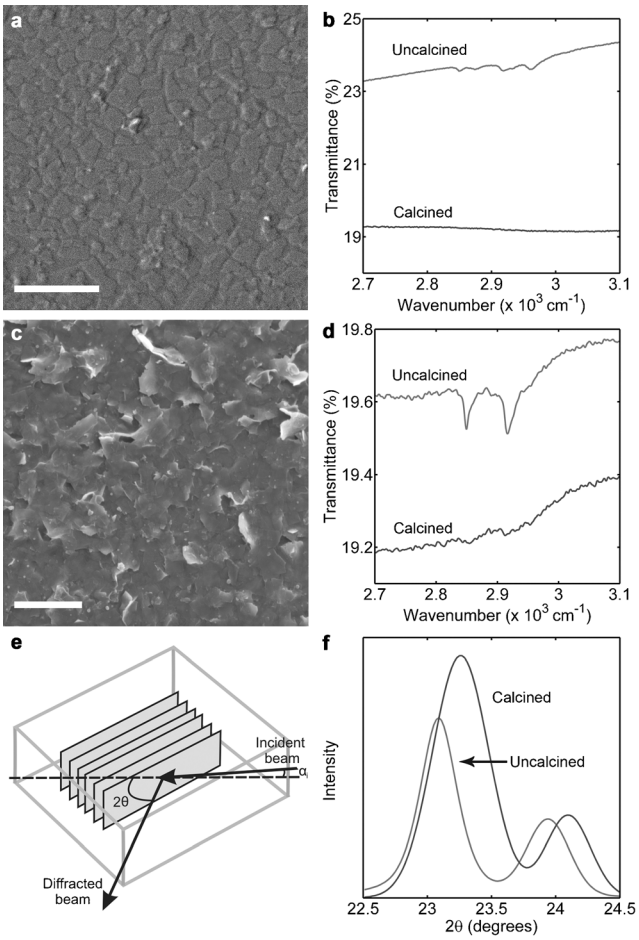

Figure 4. a,c) Single and multilayer nanosheet films made by LS; scale bars = 1 μm. b,d) FT-IR spectra obtained from nanosheet films similar to those displayed in (a,c), showing that the peaks corresponding to OSDA are absent after calcination. e) Schematic of in-plane X-ray diffraction, where α_i is the angle of incidence and 2θ is the angle between the incident beam and the detector. f) In-plane X-ray diffraction patterns obtained from a multilayer nanosheet film showing that there is in-plane contraction of the crystalline framework caused by OSDA removal on calcination.

in Figure 3b. The average thickness was measured to be 2.9 ± 0.09 nm. Almost all the nanosheets seen in Figure 3a have similar contrast, which indicates uniform thickness of the coating. A few overlapped regions are present (seen as bright spots in Figure 3a) but mostly there is monolayer coverage of nanosheets on the substrate.

The surface coverage of nanosheets could be increased by repeating LS deposition several times on the same substrate. As seen in Figure 4c, some curling was observed after 10 cycles of deposition. However, the films exhibited high coverage on the silicon substrate, compared to the single-layer coating shown in Figure 4a. Infrared spectroscopy (IR) was used to detect the presence of OSDA (Figure 4b,d). As expected, peaks corresponding to the C-H stretching mode of OSDA were observed in the region from 2800–3000 cm^{-1} for as-deposited single-layer and multilayer films, while no IR signal corresponding to the OSDA was detected after calcination at 500 °C.

Multilayer coatings of nanosheets were analyzed by in-plane X-ray diffraction (in-plane XRD), as seen in Figure 4e,f. Such an analysis could not be done for single-layer coatings because of the low signal-to-noise ratio obtained by the in-house diffractometer used. The deposited nanosheets were not intergrown but remained in contact through weak non-covalent bonding interactions (e.g., van der Waals interactions and hydrogen bonding). It was, therefore, expected that they could slide with respect to each other. Indeed, in-plane XRD revealed significant differences in the crystallographic dimensions of the deposited nanosheets before and after calcination, as shown in Figure 4f. Shifts in the (501) and (303) Bragg peaks indicated in-plane contraction of the lattice. The observed in-plane contraction of the

nanosheets is comparable to that expected from bulk silicalite-1 upon OSDA removal (Table S1).[28,29] No crack formation was detectable by SEM (Figure S4).

After calcination, the deposited monolayers were subjected to secondary growth in order to obtain intergrown films. Depending on the secondary growth procedure and conditions, distinct microstructures were obtained. Figure 5a, b show SEM images of films after secondary growth,

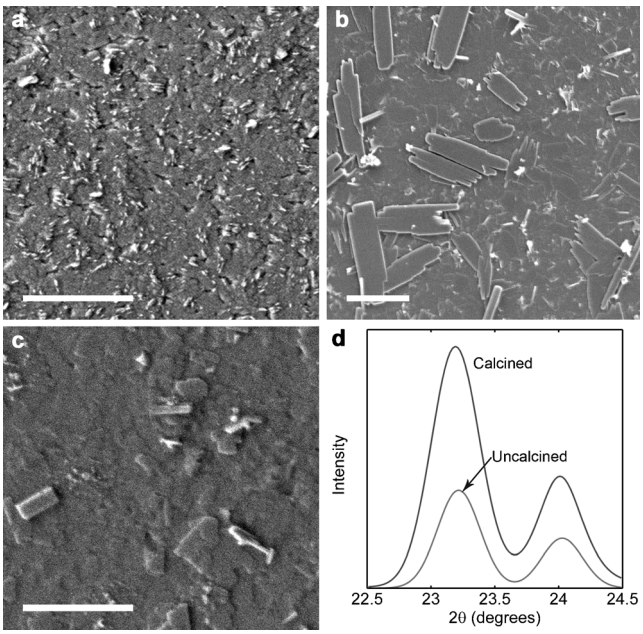

Figure 5. Secondary growth of single-layer nanosheet films using: a) TPAOH-silica sol, b) TEAOH silica gel, and c) gel-less growth using TPAOH; scale bars = 1 μm. d) In-plane X-ray diffraction before and after calcination at 500 °C obtained from the film shown in (c), indicating that there is no detectable in-plane crystallographic change caused by calcination.

carried out with the nanosheet coating in direct contact with a TPAOH-silica sol[30,31] (5 TEOS:1 TPAOH:1000 H_2O) and a TEAOH-silica gel[32] (4 TEOS:1.92 TEAOH:0.36-$(NH_4)_2SiF_6$:40 H_2O), respectively (TPAOH = tetrapropylammonium hydroxide, TEOS = tetraethylorthosilicate and TEAOH = tetraethylammonium hydroxide). In both cases, the substrates used were as-purchased silicon wafers. In the case of secondary growth using the TPAOH-silica sol, after hydrolysis and pretreatment of the sol at 150 °C, the coating was placed in it and heated to 90 °C in a sealed autoclave. After 5 h, oriented films were obtained but some twinning was seen, a common occurrence for TPAOH-silica sol-based secondary growth procedures. Specifically, oriented twins are visible in Figure 5a as thin protruding plates on the otherwise b-oriented film (see also Figure S4c). For secondary growth using the TEAOH gel method, the solid gel was aged and then mixed by a blender. Nanosheet coating was inserted into the gel and heated to 150 °C in a sealed autoclave. The morphology obtained after 6 h is shown in Figure 5b. Incomplete intergrowth was observed because of faster in-plane growth along the *c*-axis (see also Figure S4d). Further optimization of the secondary growth conditions in order to obtain thin and b-oriented films should be possible.

We also tried the "gel-less" method in which growth of MFI can be induced on a silicon wafer with oxide coating in the presence of TPAOH.[33,34] Here, the silica source is not externally introduced but comes from the substrate. Nanosheet coatings deposited on silicon substrates with a 50 nm thermally-grown oxide (which acts as the silica source) were spin-coated with a very dilute TPAOH solution and heated to a high temperature (220 °C) for 72 h. Figure 5c shows a top view SEM image of a representative film after gel-less secondary growth. An intergrown MFI zeolite layer was obtained, which remained crack-free upon calcination. Figure S5 shows additional SEM images from such films. Figure 5d shows in-plane XRD of the same film before and after calcination at 500 °C. Unlike the multilayer as-deposited films of similar thickness (see Figure 4f), the intergrown MFI films did not exhibit changes in their in-plane crystallographic dimensions. This is probably a result of strong attachment to the support and to the neighboring grains by Si-O-Si bonds. Apparently, these films were under compressive strain but remained crack free.

To determine the thickness of the films after gel-less growth, we prepared cross sections using focused ion beam (FIB) milling. The region containing Si and O was determined to be approximately 50 nm (Figure S6). This was comparable to the thickness of the SiO_2 thermal oxide layer, which was determined to be 48.8 ± 0.3 nm by ellipsometry. At this time, it was not possible to discriminate what part of this layer is SiO_2 and what part is zeolite, most likely due to amorphization of the zeolite layer by the FIB. Therefore, this technique was inconclusive in determining the exact thickness of the zeolite layer but it indicated that the film cannot be thicker than 50 nm.

To resolve the issue of zeolite film thickness, we used sparse monolayers by depositing them at low pressures (see Figure 2b). When these layers were grown using gel-less secondary growth conditions identical to those of Figure 5c, they did not cover the entire substrate. This allowed measurement of the thickness of the intergrown regions with reference to the nearby exposed substrate surface. From these measurements we determined the thickness to be less than 12 nm (Figure S7).

In summary, we report here that acid treatment of MFI nanosheets facilitated partial removal of the OSDA without altering their MFI crystal structure and thickness. This allowed for nanosheets to be dispersed in ethanol and subsequently transferred to the air–water interface. Using the Langmuir–Schaefer deposition technique, nanosheets could be transferred to solid substrates to form monolayer coatings ranging from sparse to close-packed. Successive layer-by-layer depositions resulted in oriented multilayer films with control over their thickness, while secondary growth of monolayers yielded intergrown, oriented films with sub-12-nm thickness. This unprecedented control over thickness and orientation uniformity of zeolite films may open new opportunities for investigating adsorption, transport, dielectric and mechanical properties of zeolites.

Keywords: Langmuir trough · nanosheets · surface chemistry · thin films · zeolites

How to cite: *Angew. Chem. Int. Ed.* **2015**, *54*, 6571 – 6575
Angew. Chem. **2015**, *127*, 6671 – 6675

[1] R. Hoffmann, *Angew. Chem. Int. Ed.* **2013**, *52*, 93 – 103; *Angew. Chem.* **2013**, *125*, 99 – 111.
[2] A. Corma, V. Fornes, S. B. Pergher, Th. L. M. Maesen, J. G. Buglass, *Nature* **1998**, *396*, 353 – 356.
[3] M. Choi, K. Na, J. Kim, Y. Sakamoto, O. Terasaki, R. Ryoo, *Nature* **2009**, *461*, 246 – 249.
[4] B. Marler, H. Gies, *Eur. J. Mineral.* **2012**, *24*, 405 – 428.
[5] W. Kim, S. Nair, *Chem. Eng. Sci.* **2013**, *104*, 908 – 924.
[6] H. K. Jeong, S. Nair, T. Vogt, L. C. Dickinson, M. Tsapatsis, *Nat. Mater.* **2003**, *2*, 53 – 58.
[7] P. Chlubná, W. J. Roth, H. F. Greer, W. Zhou, O. Shvets, A. Zukal, J. Cejka, R. E. Morris, *Chem. Mater.* **2013**, *25*, 542 – 547.
[8] K. Möller, T. Bein, *Science* **2011**, *333*, 297 – 298.
[9] D. Xu, G. R. Swindlehurst, H. Wu, D. H. Olson, X. Zhang, M. Tsapatsis, *Adv. Funct. Mater.* **2014**, *24*, 201 – 208.
[10] M. Tsapatsis, *Science* **2011**, *334*, 767 – 768.
[11] C. M. Lew, R. Cui, Y. Yan, *Acc. Chem. Res.* **2010**, *43*, 210 – 219.
[12] H. K. Hunt, C. M. Lew, M. Sun, Y. Yan, M. E. Davis, *Microporous Mesoporous Mater.* **2010**, *128*, 12 – 18.
[13] K. Varoon, X. Zhang, B. Elyassi, D. D. Brewer, M. Gettel, S. Kumar, J. A. Lee, S. Maheshwari, A. Mittal, C. Sung, M. Cococcioni, L. F. Francis, A. V. McCormick, K. A. Mkhoyan, M. Tsapatsis, *Science* **2011**, *334*, 72 – 75.
[14] K. V. Agrawal, B. Topuz, Z. Jiang, K. Nguenkam, B. Elyassi, M. Navarro, L. F. Francis, M. Tsapatsis, *AIChE J.* **2013**, *59*, 3458 – 3467.
[15] K. B. Blodgett, *J. Am. Chem. Soc.* **1934**, *56*, 495.
[16] I. Langmuir, V. J. Schaefer, *J. Am. Chem. Soc.* **1938**, *60*, 1351 – 1360.
[17] M. C. Petty, *Langmuir-Blodgett Films An Introduction*, Cambridge University Press, Cambridge, **1996**, pp. 39 – 64.
[18] K. Morawetz, J. Reiche, H. Kamusewitz, H. Kosmella, R. Ries, M. Noack, L. Brehmer, *Colloids Surf. A* **2002**, *200*, 409 – 414.
[19] L. Tosheva, V. P. Valtchev, B. Mihailova, A. M. Doyle, *J. Phys. Chem. C* **2007**, *111*, 12052 – 12057.
[20] Z. Wang, L. H. Wee, B. Mihailova, K. J. Edler, A. M. Doyle, *Chem. Mater.* **2007**, *19*, 5806 – 5808.
[21] L. H. Wee, Z. Wang, L. Tosheva, L. Itani, V. Valtchev, A. M. Doyle, *Microporous Mesoporous Mater.* **2008**, *116*, 22 – 27.
[22] J. Li, X. Liu, X. Lv, B. Zhang, *Mater. Lett.* **2014**, *124*, 299 – 301.
[23] R. Makiura, S. Motoyama, Y. Umemura, H. Yamanaka, O. Sakata, H. Kitagawa, *Nat. Mater.* **2010**, *9*, 565 – 571.
[24] L. Imperiali, K.-H. Liao, C. Clasen, J. Fransaer, C. W. Macosko, J. Vermant, *Langmuir* **2012**, *28*, 7990 – 8000.
[25] A. Corma, U. Díaz, T. García, G. Sastre, A. Velty, *J. Am. Chem. Soc.* **2010**, *132*, 15011 – 15021.
[26] P. Kumar, K. V. Agrawal, K. A. Mkhoyan, M. Tsapatsis, *Nat. Commun.*, in press.
[27] L. A. Nagahara, K. Hashimoto, A. Fujishima, D. Snowdenlfft, P. B. Price, *J. Vac. Sci. Technol. B* **1994**, *12*, 1694 – 1697.
[28] X-ray powder diffraction data for bulk silicalite-1 can be found at http://www.iza-online.org.
[29] E. Geus, H. Van Bekkum, *Zeolites* **1995**, *15*, 333 – 341.
[30] T. M. Davis, T. O. Drews, H. Ramanan, C. He, J. Dong, H. Schnablegger, M. A. Katsoulakis, E. Kokkoli, A. V. McCormick, R. L. Penn, M. Tsapatsis, *Nat. Mater.* **2006**, *5*, 400 – 408.
[31] Y. Liu, Y. Li, W. Yang, *J. Am. Chem. Soc.* **2010**, *132*, 1768 – 1769.
[32] T. C. T. Pham, H. S. Kim, K. B. Yoon, *Science* **2011**, *334*, 1533 – 1538.
[33] W. Chaikittisilp, M. E. Davis, T. Okubo, *Chem. Mater.* **2007**, *19*, 4120 – 4122.
[34] T. C. T. Pham, T. H. Nguyen, K. B. Yoon, *Angew. Chem. Int. Ed.* **2013**, *52*, 8693 – 8698; *Angew. Chem.* **2013**, *125*, 8855 – 8860.

Received: December 8, 2014
Published online: April 13, 2015

